# *The effect of horizontal resolution on the representation of the global monsoon annual cycle in Atmospheric General Circulation Models*

Article

Accepted Version

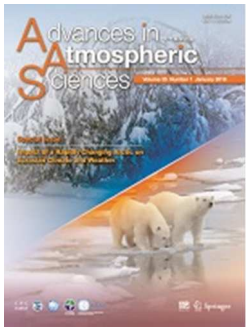

# The effect of horizontal resolution on the representation of the global monsoon annual cycle in Atmospheric General Circulation Models



| | |
|---|---|
| Journal: | *Advances in Atmospheric Sciences* |
| Manuscript ID | AAS-2017-0273.R1 |
| Manuscript Type: | Special Issue: CSSP (Submission deadline: 31 Oct. 2017) |
| Date Submitted by the Author: | n/a |
| Complete List of Authors: | Zhang, Lixia; IAP, LASG<br>ZHOU, Tian-Jun; IAP, LASG<br>Klingaman, Nicholas; University of Reading, National Centre for Atmospheric Science and Department of Meteorolog<br>Wu, Peili; Met Office, Hadley Centre<br>Roberts, Malcolm J.; Met Office, Hadley Centre |
| | |

# The effect of horizontal resolution on the representation of the global monsoon annual cycle in Atmospheric General Circulation Models

Lixia Zhang[1, 2], Tianjun Zhou[1], Nicholas P. Klingaman[3], Peili Wu[4], Malcolm Roberts[4]

[1]*LASG, Institute of Atmospheric Physics, Chinese Academy of Sciences, Beijing, China*

[2]*Collaborative Innovation Center on Forecast and Evaluation of Meteorological Disasters, Nanjing University of Information Science & Technology, Nanjing, China*

[3]*National Centre for Atmospheric Science and Department of Meteorology, University of Reading, Reading, United Kingdom*

[4.] *Met Office Hadley Centre, Exeter, United Kingdom*

***Submitted to AAS CSSP special issue***

*Revised on Jan, 2018*

**Corresponding author:**

Dr. Lixia Zhang

LASG, Institute of Atmospheric Physics, Chinese Academy of Sciences,

Beijing 100029, China.

Phone: 86-10-8299-5452

Fax: 86-10-8299-5172

Email: lixiazhang@mail.iap.ac.cn

## Abstract

The sensitivity of the representation of the global monsoon annual cycle to horizontal resolution is compared in three Atmospheric General Circulation Models (AGCMs): the Met Office Unified Model-Global Atmosphere 3.0 (MetUM-GA3), the Meteorological Research Institute AGCM3 (MRI-AGCM3) and Global High Resolution AGCM from the Geophysical Fluid Dynamics Laboratory (GFDL-HiRAM). For each model, we use two horizontal resolution configurations for the period 1998–2008. Increasing resolution consistently improves simulated precipitation and low-level circulation of the annual mean and the first two annual cycle modes, as measured by pattern correlation coefficient and Equitable Threat Score. Improvements in simulating the summer monsoon onset and withdrawal are region-dependent. No consistent response to resolution is found in simulating summer monsoon retreat. Regionally, increased resolution reduces the positive bias in simulated annual mean precipitation, the two annual-cycle modes over the West African monsoon and Northwestern Pacific monsoon. An overestimation of the solstitial mode and an underestimation of the equinoctial asymmetric mode of the East Asian monsoon are reduced in all high-resolution configurations. Systematic errors exist in lower-resolution models for simulating the onset and withdrawal of the summer monsoon. Higher resolution models consistently improve the early summer monsoon onset over East Asia and West Africa, but substantial differences exist in the responses over Indian monsoon region, where biases differ across the three low-resolution AGCMs. This study demonstrates the importance of a multi-model comparison when examining the added value of resolution and the importance of model physical parameterizations for the Indian monsoon simulation.


**Key Words**：global monsoon, high resolution modeling, annual cycle, AMIP

## 1. **Introduction**

Monsoons are characterized by a seasonal wet-dry contrast and a reversal of prevailing winds, due to the reversal of land-sea and inter-hemispheric thermal contrasts forced by the annual cycle of solar heating. The global monsoon is a dominant mode of annual variability of the global tropical circulation and is a response of the coupled climate system to annual variations in solar forcing (Wang and Ding 2008). Global monsoon regions sustain nearly two-thirds of the world's population and support some of the largest and fastest growing urban areas. The simulation and prediction of the annual cycle of monsoon circulation and precipitation is critically important, because of the effect of monsoons on hydrology, agriculture and local livelihoods and economies.

Although global monsoon regions are connected through mass conservation (Trenberth et al. 2000), each regional monsoon has unique characteristics due to the local interactions among the land surface, ocean, convection and synoptic weather systems, especially over Asian-Australian monsoon region. The well-recognized Asian summer monsoon system typically first onsets over the Bay of Bengal (BoB) in early May, followed by the South China Sea in mid-May and then India in early June (Wu and Zhang 1998; Xu and Chan 2001; Mao and Wu 2007). The onset over the BoB is often preceded by the development of a monsoon onset vortex (Krishnamurti and Ramanathan 1982; Wu et al. 2012). A numerical study by Liu et al. (2002) demonstrated that the onset of South China Sea monsoon is due to a Rossby wave train triggered by the strong latent heating during the BoB monsoon onset. The seasonal march of the East Asian summer monsoon (EASM) displays a stepwise northward and northeastward advance. From early May to mid-May, the ridge line of the western Pacific subtropical high (WPSH) is located along 15°N, and southern China experiences a pre-monsoon rainy season. Later, the WPSH exhibits two northward jumps in June and July with the ridge line located at 20ºN and 25ºN, respectively, the monsoon

rain band extends abruptly from the Indochina Peninsula – the South China Sea – from the Philippines to the Yangtze River valley in early to mid-June, and the Meiyu (or Baiu in Japan and Changma in Korea) begins. The monsoon penetrates into northern China (34-41ºN) in mid-July, and the monsoon rainy season there lasts for one month and ends in early-middle August (Zhou et al. 2009). For the Australian summer monsoon onset in December, there are four major contributing factors, including land-sea thermal contrast, barotropic instability, arrival of the Madden-Julian oscillation (MJO) and intrusion of a mid-latitude trough (Hung and Yanai 2004). The mean onset of the summer monsoon over West Africa is 24th June, which is linked to an abrupt latitudinal shift of the Inter-Tropical Convergence Zone (ITCZ) from a quasi-stationary location at 5˚N in May-June to another quasi-stationary location at 10˚N in July-August (Sultan and Janicot 2003). For American summer monsoon, the northward rainbelt movement over southwestern North America from mid-to-late June is associated with the northward progression of the ITCZ (Yu and Wallace 2000; Higgins and Shi 2001), while the onset of South American monsoon is related to eastward displacement of the South Atlantic subtropical high; it is also affected by intraseasonal variability through low-frequency trough or ridge occurrence over southern Brazil (Raia et al. 2008). The unique features of regional monsoons and their onset have been rigorous metrics for gauging climate models' performances.

The complexity of monsoon systems presents great challenges to simulate the climatological seasonal means and annual cycles of the monsoon (Sperber et al. 2013; Zhou et al. 2017), although substantial efforts have been made to improve model physics and dynamics in the past several decades. Model biases in the simulation of the monsoons limit the fidelity of monsoon predictions and projections (Dong et al. 2016). Sperber et al. (2013) evaluated the performance of 25 coupled climate models from Coupled Model Intercomparison Project Phase 5 (CMIP5) and 22 models from CMIP Phase 3 (CMIP3) in simulat-

ing the Asian summer monsoon onset and retreat. The authors found an overall delayed onset over India in models, even though CMIP5 models showed improved fidelity relative to CMIP3. The onset and retreat definition in Sperber et al. (2013) was based on rainfall thresholds; monsoon onset might not occur in models, or may be delayed relative to observations, because of systematic dry biases. To avoid this issue, Sperber and Annamalai (2014) proposed a fractional accumulation method to evaluate the monsoon annual cycle; this method can be applied to many monsoon domains. The authors also found some systematic errors in the phase of rainfall annual cycle: coupled climate models in CMIP5 have delayed onsets of summer rainfall over India, the Gulf of Guinea, and South America, but early onsets for the Sahel and the North America.

Several studies have proposed techniques to improve monsoon simulation, including increasing horizontal resolution to capture more realistic large-scale atmospheric circulations and precipitation distributions (Hack et al. 2006; Roberts et al. 2009; Demory et al. 2014；Berckmans et al. 2013). The added value of resolution in GCMs has been widely verified for many aspects of monsoon simulation (Kitoh et al., 2008; Mizuta et al., 2012; Johnson et al., 2016). For example, an examination of version 5.1 of the National Center for Atmospheric Research Community Atmosphere Model (CAM5) at three resolutions showed a much better representation of the intensity-frequency structures of precipitation in steep-terrain regions over East Asia (Li et al. 2015). Higher resolution in CAM5 also improves the simulation of East Asian summer monsoon rain belt (Yao et al. 2017). Most investigations of the benefits of increased resolution were based on one model, however the sensitivity to resolution may differ among models. Ogata et al. (2017) showed that the MRI-AGCM3 and the MetUM-GA3 produced less precipitation over the western Pacific with increasing resolution, but their sensitivity of Indian Ocean precipitation to resolution differed. Zhang et al. (2017) compared three AGCMs, each with two resolution configura-

tions, and showed the sensitivity of monsoon precipitation to resolution varied greatly among the models. To understand what aspects of resolution sensitivity are common among AGCMs, it is important to compare several AGCMs using the same metrics. Given the social and scientific importance of the onset and cessation of monsoon precipitation to local livelihoods and economies, it is desirable to find whether high resolution systematically improves the representation of monsoon onset and withdrawal. This is the major motivation of the current study.

The remainder of the paper is organized as follows. The model simulations, validation data and evaluation metrics are described in section 2. The improvement of high resolution in simulating the annual cycle modes and summer monsoon onset and withdrawal are assessed in section 3 and 4, respectively. Section 5 presents the summary and discussion.

## 2. Models, data and method description

### 2.1 Model simulations and observational validation datasets

We use daily precipitation and monthly wind data from simulations with three AGCMs, MetUM-GA3, MRI-AGCM3 and GFDL-HiRAM, each with two resolution configurations for the period 1998–2008. Details of the models and experiments can be found in Table 1. The model outputs of GFDL-HiRAM and MRI-AGCM3 were obtained from the Coupled Model Intercomparison Project phase 5 data archive (Taylor et al., 2012). The simulations of MetUM-GA3 are from the UPSCALE (UK on PRACE: weather-resolving Simulations of Climate for globAL Environmental risk) project (Mizielinski et al., 2014). There are very few different physical and dynamical settings in the MetUM-GA3 high-resolution configuration compared to its low-resolution counterparts, mostly related to numerical stability (Table 2 in Mizielinski et al. 2014). There are no physical parameter adjustments between the MRI-AGCM3-2H and MRI-AGCM3-2S (Endo et al. 2012; Kusunoki 2016). In GFDL-HiRAM, the shallow convective scheme and cloud microphysics are changed in

C360 from C180 (Zhao et al. 2009; Chen and Lin 2012). We analyze the ensemble mean of all realizations of each model. Because of the large inter-model differences in dynamical cores and physics, it is hard to compare the resolution sensitivity across models. To exclude the impact of model dependence and focus more on resolution, we compared the high- and low-resolution configurations of the each model in this study.

The observed daily precipitation datasets used in this study include (1) Tropical Rainfall Measuring Mission (TRMM) 3B42 V7 (Huffman et al. 2007), to evaluate the climatological mean state of global monsoon precipitation, at 0.25˚x0.25˚ resolution; and (2) Global Precipitation Climatology Project V1.2 (GPCP), with a resolution 1.0˚x1.0˚ (Adler et al. 2003). In addition, monthly wind data from Climate Forecast System Reanalysis (CFSR; Saha et al. 2010) with a resolution of 0.5˚x0.5˚ and from National Centers for Environmental Prediction–National Center for Atmospheric Research (NCEP–NCAR) reanalysis with a resolution 2.5˚x2.5˚ (Kalnay et al. 1996) are used as the circulation datasets. All datasets are interpolated to the N216 resolution of MetUM-GA3 (approximately 0.83°longitude×0.55° latitude) using a distance-weighted interpolation method, to facilitate comparison. The longest common period of 1998-2008 covered by all simulations and observations is selected in the following analysis.



### 2.2 Evaluation metrics on global monsoon annual cycles

In this study, two aspects of the annual cycle of the global monsoon are evaluated: (1) the mean climate and annual cycle modes and (2) monsoon onset and withdraw. As proposed by Wang and Ding (2008), the annual mean, the solstitial (symmetric) and equinoctial (asymmetric) modes of the annual cycle, and the global monsoon domain can be used as metrics to gauge model performance for simulating the mean climate and annual cycle. The solstitial mode is represented by the differences in precipitation or circulation between

June-September and December–March means; the equinoctial asymmetric mode is represented by the differences between April-May and October-November. The global monsoon domain is delineated both by the monsoon precipitation index (MPI) and zonal westerly wind index (MWI). MPI is defined as the annual range of precipitation normalized by its annual mean. MWI is similar, but using 850 hPa zonal wind (U850). The monsoon precipitation domains are the areas where the annual range of precipitation exceeds 300mm and MPI exceeds 0.5, whereas monsoon wind domains are defined as WMI exceeding 0.5 without any restriction on the magnitude of annual range. The Annual range is the difference between May-September (MJJAS) and November-March (NDJFM) means in the Northern Hemisphere, or NDJFM minus MJJAS in the Southern Hemisphere.

Previous studies have proposed several definitions of monsoon onset and withdrawal. The commonly used definition is threshold-based (Wang and Lin 2002). One of the weaknesses of the threshold-based techniques is that monsoon onset might be delayed or accelerated by dry or wet biases, respectively, in the model, even though the model may have a realistic annual cycle amplitude (Sperber et al. 2013; Sperber and Annamalai 2014). Models with dry biases are especially at a disadvantage since the observed threshold for defining monsoon may never be reached in such models, including MetUM-GA3 in this study (Bush et al. 2015; Johnson et al. 2016). Since the biases differ among the three models used here, it is important to find a relatively fair way to evaluate onset and withdrawal in models. Thus, a fractional accumulation approach is employed here. The monsoon onset and withdrawal are defined as the pentad when the fractional accumulation first becomes >=0.2 and >=0.8, respectively (Sperber and Annamalai 2014). The fractional accumulated precipitation in a given pentad is the accumulated rainfall at that pentad divided by the total accumulated rainfall at the end of the year. In this study, the pentads for the

Southern African, Australian and South American domains have been reordered to run from July 2 to June 27.

To quantitatively show the sensitivity of the simulated monsoon domain to resolution, the Equitable Threat Score (ETS, Jolliffe and Stephenson 2003) is used in this study to measure the simulation skill of the monsoon domain, which can be evaluated as a binary event.

$$ETS=(a-ar)/(a+b+c-ar) \quad (1)$$

where $ar=(a+b)(a+c)/n$, represents the skill of a random prediction. a, b, and c are the counts of hits, false alarms and misses of monsoon domain, respectively, and n is the number of model gridpoints in the region (45°S-45°N). The definition of each variable in equation (1) can be found in Table 2. ETS ranges from 0 to 1 with perfect score of 1.

## 3. Annual mean and annual cycle modes

To investigate whether the improvement from higher-resolution is consistent across the three models, we analyze the biases in the lower-resolution configuration and the differences between the high- and low- resolution configurations. The bias in simulated annual mean precipitation and improvements from higher resolution are presented in Fig.1. In observations (blue lines in left panel of Fig.1), substantial precipitation falls in the Indo-Pacific warm pool (60˚E-180˚), ITCZ and South Pacific Convergence Zone (SPCZ). In general, the observed centers are well captured by the low-resolution configuration of each AGCM, with an overall positive bias over most of the tropics (blue lines in right panel of Fig.1). In contrast, there are several common biases among the three low-resolution AGCMs, including overestimations over the southwest Indian Ocean, SPCZ, northern edge of the ITCZ, and Northwestern Pacific Ocean, with underestimations over the southeastern Indian Ocean (Fig.1 a, c, e). Unique biases in each AGCM are also found, particularly in

MetUM-GA3 N216, which underestimates Indian and Maritime Continent precipitation (Fig.1a). A positive bias over the western central Pacific (5˚S-5˚N, 120˚E-180˚) is seen in MRI-AGCM3-2H, while negative biases are present in MetUM-GA3 N216 and GFDL-HiRAM-C180. A consistent response to higher resolution among the three models is suppressed precipitation over the north of Maritime Continent (MC) and western Pacific (5˚S-15˚N, 120˚-160˚E), which partly reduces the wet bias over the Northwestern Pacific (5˚-15˚N, 120˚-160˚E) in the three low-resolution models. This consistent response to finer resolution also has been illustrated by Ogata et al. (2017), which compared MetUM-GA3 and MRI-AGCM3. This is further verified with one additional model, GFDL-HiRAM. As suggested by Ogata et al. (2017) and Johnson et al. (2016), the reduced precipitation over the north of MC and western Pacific may be related to better-resolved steep topography over MC and Indochina, with moisture convergence and precipitation on the windward side of the orography, which leads to decreased moisture availability on the leeward side in summer and reduced precipitation over the north of MC and western Pacific. This can be partly seen from the difference between higher- and lower-resolution models in simulating the solstitial mode in Fig.2. Note that the low-resolution of both MetUM-GA3 and GFDL-HiRAM underestimate the precipitation over MC, and the consistent response to resolution makes this dry bias even worse.

As in Fig. 1, the biases in low-resolution models and improvement in higher- resolution configurations for the solstitial mode are shown in Fig. 2. The observed spatial pattern shows an asymmetric contrast, with positive centers in Northern Hemisphere monsoon regions (Indian-Pacific-East Asia, West Africa and northeast tropical Pacific (5˚-20˚N, 120˚-60˚W)) and negative centers in Southern Hemispheric monsoon regions (South Africa, Australia and South America; lines in left panel of Fig.2). The centers are well reproduced by all low-resolution models, but all show underestimations over East Asia, the northeast

tropical Pacific, South Africa and Australia region and overestimations over the northwest Pacific (shading in left panel of Fig.2). Higher resolution reduces this consistent simulation bias, particularly over the northwest Pacific and northeast tropical Pacific (shading in left panel of Fig.2). The improvement, however, is far smaller than the low-resolution model bias. The biases in the three low-resolution models differ greatly over the Indian monsoon region, where the solstitial mode is dramatically smaller than observation in MetUM-GA3 N216, greater in MRI-AGCM3-2H, and close to observation in GFDL-HiRAM-C180. The sensitivity of the solsticial mode in each model to resolution also differs over the Indian monsoon region. The inconsistency of model biases and sensitivity to resolution indicate the strong role for sub-grid scale physical parameterizations for simulating the Indian monsoon precipitation.

The biases in the simulated equinoctial asymmetric mode of the annual cycle and corresponding improvements in high-resolution models are shown in Fig. 3. In observations, negative values are centered in the zonal belt along (10˚N-20˚N), while positive values are centered to its south (0˚-10˚N) and in Southeast China. The centers over the Pacific represent the asymmetric location of the spring and fall ITCZ (Wang and Ding 2008). The positive values over Southeast China shows the region's characteristic spring-persistence season in April and May (Li et al. 2017). All low-resolution models capture the asymmetric pattern of spring and fall precipitation, but a systematic overestimation over the Northern Hemisphere is seen in all models, with negative biases north of the observed negative center and positive biases near the observed positive centers. Positive biases over West Africa are found in all low-resolution models. In high-resolution models, the overestimation over Northwestern Pacific, West Africa and Southeast China is suppressed in all models; consistent improvements are also found over the southern Maritime Continent. This indicates increased resolution improves simulated precipitation in transition seasons.

To quantify the improvement in high-resolution models, the pattern correlation coefficient (PCC) and root-mean-square-error (RMSE) of simulated precipitation over (45˚S-45˚N) against TRMM are shown in Fig.4 a,d,g. The simulated 850 hPa winds for the annual mean and the first annual cycle modes against CFSR reanalysis are also presented in Fig.4. We compare the metrics for GPCP against TRMM and for NCEP-NCAR against CFSR to show the observational uncertainty. In general, all low-resolution models simulate well the observed precipitation and 850 hPa wind patterns. For example, the PCCs (RMSEs) of simulated annual mean precipitation and 850 hPa zonal (U850) and meridional wind (V850) in low resolution models (blue markers in Fig.4a-c) range from 0.85 to 0.90 (1.2 to 1.6 mm/day), 0.97 to 0.99 (0.75 to 1.2 m/s) and 0.88 to 0.94 (0.47 to 0.60 m/s), respectively, which are close to those PCCs for GPCP and NCEP-NCAR against TRMM and CFSR, respectively. The PCCs increase consistently in all three high-resolution models (red markers) compared with their low-resolution counterparts (blue markers) for the three annual-cycle metrics. However, the model bias as demonstrated by RMSE appears insensitive to increasing resolution. The PCCs of annual precipitation, U850, V850 simulated by high-resolution models are systematically shifted to right of the low-resolution ones, increasing to 0.95~0.97, nearly 1.0 and 0.96~0.98, respectively. The PCCs in high-resolution models are even higher than PCCs of GPCP/NCEP-NCAR, although the RMSEs in these simulations are far larger than the reanalysis. The same results are also found in the first two leading modes. High resolution aids in representing details of precipitation and circulation distributions, but not in reducing model biases.

Following the global monsoon domain definition proposed by Wang and Ding (2008), the distributions of precipitation annual range and monsoon domain based on precipitation are obtained and shown in Figure 5. In TRMM, the monsoon systems are well depicted by this definition, including the Asian–Australian monsoon, the North and South African

monsoons, and the North and South American monsoons (Fig.5a). The domain obtained from GPCP is similar to TRMM except at the edges, particularly over the northern edge of the northwestern Pacific monsoon region and the southern edge of the southwestern Indian Ocean monsoon region, where the domain areas are relatively larger in GPCP than in TRMM. The North American monsoon region (120˚W-60˚W, 0˚-20˚N) in all low-resolution models is smaller and the western boundary is about 30 degrees eastward shifted relative to observations, while the simulated northwestern Pacific monsoon is wider and stronger than observations (left column in Fig.5). With increased resolution, the northwestern Pacific monsoon region shrinks relative to the low-resolution models, particularly for MRI-AGCM3, which extends to 170˚W in MRI-AGCM3-2H but only to 170˚E in MRI-AGCM3-2S. Each model has unique biases, such as the absence of the Indian monsoon region in MetUM-GA3 N216 due to its dry bias in India, a westward extended West African monsoon (60˚W-60˚E, 0˚-20˚N) in MetUM-GA3 N216 and MRI-AGCM3-2H due to a wider and stronger ITCZ over the Atlantic Ocean, and an unrealistic monsoon region over the southern tropical Atlantic Ocean in MRI-AGCM3-2H and GFDL-HiRAM-C180. Those biases remain in their high-resolution counterparts, indicating little influence of resolution increase. Similar analysis of the global monsoon domain based on U850 revealed no obvious improvements from increased resolution (Figure not shown).

To quantitatively show the sensitivity of the simulated monsoon domain to resolution, the Equitable Threat Score (ETS, Jolliffe and Stephenson 2003) for global and individual regional monsoon domains was computed, using precipitation and U850 (Figure 6). Generally, higher-resolution configurations show slightly increased ETS for global monsoon precipitation (wind): from 0.53 to 0.54 (0.63 to 0.67) in MetUM-GA3, 0.56 to 0.57 (0.68 to 0.69) in GFDL-HiRAM and 0.58 to 0.62 (0.73 to 0.77) in MRI-AGCM3 models, respectively. The ETS of the three high-resolution models for regional monsoon precipitation

domains are not always higher than their low-resolution counterparts. Consistent improvements with resolution are shown only for the South African monsoon domain, with the largest increase from 0.59 to 0.64 in MetUM-GA3. The ETS for regional monsoon wind domains are all higher in the high-resolution configurations. Note that the ETS metrics of U850 and precipitation are not correlated. The skill scores of U850 are higher than those of precipitation for both global and regional monsoons. Even though the higher-resolution models show increased ETS for U850 for all regional monsoons except the East Asian monsoon, the ETS metrics for precipitation do not increase (e.g., for the Indian monsoon).

## 4. Monsoon onset and withdrawal

Cumulative rainfall, which is the sum of rainfall up to a given pentad, averaged over each monsoon region is presented in Fig.7 to show the temporal characteristics of the rainfall and the model bias. A rapid increase in cumulative occurs in all monsoon regions. However, the initial pentad for the rapid increase differs among regions, indicating different onset times in each region. For the Asian-Australian monsoon system, rapid precipitation increase starts around pentad 30 in India, pentad 25 in Southeast Asia and East Asia, and pentad 10 in Australia. Over the African and American monsoon systems, an onset is observed in the pentad 30 in West Africa and North America, and pentad 5 in South Africa and South America.

An overall overestimation of annual total precipitation is presented over all regional monsoons except for India and Southeast Asia. For Indian monsoon, there is a large disparity among the models in simulated total rainfall. There is an obvious wet bias (50% wetter than TRMM) in MRI-AGCM3, a dry bias (50% less than TRMM) in MetUM-GA3 AGCMs and a relatively small bias in GFDL-HiRAM (Fig. 7a). The biases over Southeast Asia are similar to those over India, but with smaller magnitudes (Fig. 7b). The evolution of precipitation accumulation shows that the bias is relatively small in the beginning of

year, but starts to increase around the monsoon onset pentad.

The observed and simulated spatial distributions of monsoon onset are shown in Fig.8. The monsoon onset is the pentad when fractional accumulation first becomes >=0.2 (Sperber and Annamalai 2014). We also examined the distributions of monsoon onset defined by Wang and Lin (2002), in which onset is determined as the first pentad with the relative rainfall rate to January mean in NH and July in SH exceeds 5 mm $d^{-1}$. This threshold is never reached in MetUM-GA3 over India because of the systematic dry bias (Fig.1, Fig. 2 and Fig.7a). However, India is defined as a monsoon region in MetUM-GA3 based on the monsoon wind index (Figure not shown). Thus, it is reasonable to use the fractional accumulation to define monsoon onset and withdrawal. To focus on monsoon regions, only the distributions in the observed monsoon regions based on the monsoon precipitation index are shown here. In observations (Fig.8a-b), the onset pentad shows a gradual increase from the equator to poleward, indicating later onset in the higher-latitude monsoon regions in both hemispheres. In the NH, the earliest onset is pentad 25 in early May over the southern edge of the Northern Hemispheric monsoon region and South China, while in the SH the earliest onset is pentad 68 in early December over the northern edge of Southwest Indian Ocean. The latest NH monsoon onset is at pentad 47 in mid-August over the northern edge of the North American and West African monsoons (pentad 15 in mid-March over the south edge of Australian monsoon in SH).

All models simulate well the spatial distribution of global summer monsoon onset. However, all low-resolution models simulate earlier monsoon onsets than the two observed datasets, such as over the East Asian, West Africa monsoon, North American and South American monsoon. Specifically, the area with onset by pentad 25 (hereafter P25 area) over the West African, North American and East Asian monsoons is broader than in the observation. In the high-resolution models, the P25 area slightly shrinks over the East

Asian and Western African monsoons, particularly apparent in MetUM-GA3. This difference is also seen in the observations, in which the P25 area in GPCP is larger than in TRMM, potentially due to the different resolutions of two observed datasets. It indicates that high resolution improves the spatial distribution of precipitation and the delineation of the monsoon onset boundaries. In other monsoon regions, there are no clear advantages of increased resolution.

As for the global monsoon onset, we compute distributions of monsoon withdrawal, the pentad with fractional accumulation first becomes >=0.8, in simulations and observations (Fig. 9). The observed monsoon withdraws from higher latitudes toward the equatorial monsoon regions. In NH, the earliest withdrawal over East Asian monsoon is witnessed at pentad 48 in late August; the latest is over the southern edge of the Northern Hemispheric monsoon region at pentad 60 in late October. In the SH, the earliest is over South Africa at pentad 14 in mid-March and the latest over northern edge of Australia at pentad 30 in late June. The observed monsoon withdrawal patterns are well captured by all models, but with relatively later withdrawals over the Australian and North American monsoons by two pentads. There are no obvious differences between the low- and high-resolution configurations, or between GPCP and TRMM. These results suggest monsoon withdrawal is less sensitive to resolution than monsoon onset.

To quantitatively identify the improvements from higher resolution, the summer monsoon onset and withdrawal pentads averaged over each regional monsoon are shown in Figure 10. In observations, TRMM shows (red dots in Fig. 10) that the monsoon onsets (withdraws) at pentad 33 (52) over India, 30.5 (54) over Southeast Asia, 27.5 (49.5) over East Asia, 7 (28.5) over Australia, 32.8 (53.5) over West Africa, 8.2 (27) over South Africa, 32.4 (56) over North America and 3.2 (27.2) over South America, respectively. Compared with TRMM, the onset pentads of all regional monsoons except the Indian monsoon

are systematically earlier in GPCP, the lower-resolution observational dataset, with the largest difference of up to two pentads earlier in the West Africa monsoon. However, the monsoon withdrawal dates from TRMM and GPCP are similar, with a maximum difference of 0.5 pentad. The difference between TRMM and GPCP may suggest that resolution has greater impact on monsoon onset than on withdrawal. For all domains the model dispersion far exceeds the differences between TRMM and GPCP. Here, we use the onset and withdrawal derived from TRMM as a reference due to its higher resolution than GPCP. All models show earlier onsets over East Asia, West Africa, South Africa and North America. The results are consistent with Fig.8 and Fig.9. Specifically, the largest bias is about 4.5 pentads in MRI-AGCM3-2H over East Asia, 4 pentads in GFDL-HiRAM-C180 over West Africa, 2 pentads in GFDL-HiRAM-C360 over South Africa and 4.5 pentads in GFDL-hIRAM-C360 over North America, respectively. Increased resolution consistently delays the monsoon onset over East Asia and West Africa in all AGCMs, matching well with the differences between TRMM and GPCP. However, these improvements from high resolution are only one pentad at most, far less than the biases of the corresponding low-resolution models (≤4.5 pentad). A consistently slightly advanced onset in higher-resolution models (1.5 pentad earlier at maximum over Southeast Asia) relative to their lower-resolution counterparts is shown over Southeast Asia, Australia, South Africa, North America and South America. For the Indian monsoon, both the biases of the lower-resolution configurations and the improvement in the high-resolution configurations differ greatly among the three AGCMs, indicating less resolution sensitivity of Indian monsoon onset.

## 5. Summary and discussion

In this study, the resolution sensitivity of the annual cycle of the global monsoon is investigated in three AGCMs, MetUM-GA3, MRI-AGCM3 and GFDL-HiRAM. We com-

pared output from MetUM-GA3 at N216 (90-km) and N512 (40-km), MRI-AGCM3-2H (60-km) and MRI-AGCM3-2S (20-km), and GFDL-HiRAM-C180 (65-km) and GFDL-HiRAM-C360 (32-km). We found consistent and inconsistent responses across the three AGCMs to increasing resolution.

A summary plot about the model responses to horizontal resolution is presented in Fig.11. All low-resolution AGCMs are biased toward higher annual mean precipitation and stronger solstitial and equinoctial asymmetric modes. With increasing resolution, all AGCMs show consistent improvements in simulating the precipitation and low-level circulation of the annual mean and the first two annual cycle modes, as determined from the pattern correlation coefficient and ETS as denoted by red boxes in Fig.11. Regionally, higher pattern correlation coefficients are found in three high-resolution AGCMs for precipitation for the annual mean (ANN), solstitial mode (AC1) and the equinoctial asymmetric mode (AC2) for all regional monsoons, except the Australian (Aus) and North American monsoons (NAm). The inconsistent response to increased resolution across the three AGCMs over North American and Australian monsoons may be partly due to their small monsoon area.

We found that improvements in simulating the summer monsoon onset and withdrawal are regionally dependent. No consistent response to resolution is found in simulating monsoon withdrawal. A consistent improvement in simulating East Asian (EAs), Southeast Asian (SAs) and Western African (WAf) monsoon onset are shown across three AGCMs, by delaying the monsoon onset over EAs and WAf and advancing over SAs. A consistently weakened equinoctial asymmetric mode over EAs and WAf with increasing resolution is seen across the three models, reducing wet biases in the transition seasons. Thus, the summer monsoon onset pentad of the two regional monsoons is systematically delayed in all high-resolution models relative to their low-resolution counterparts. In contrast, the im-

provements of monsoon onset over SAs are consistently advanced across three models. Systematic errors and responses to resolution differ greatly across the three AGCMs for the simulated Indian (India) North American (NAm) and South hemispheric regional monsoons (Aus, SAf, SAm), and the response to resolution differs across the three AGCM, indicating the dependence of these regions on physical parameterizations. Nevertheless, better representation on the Indian are shown in all three AGCMs.

Comparing the impact of resolution on the simulated regional monsoon precipitation annual cycle, this study demonstrates the importance of resolution for the East Asian monsoon and West African monsoon where improved annual cycles are simulated in the three AGCMs. The positive bias of AC2 over the West African monsoon region is caused by overestimated precipitation in spring; in CMIP5 models, this bias has been linked to the representation of African Easterly Waves (see Fig.6 in Martin and Thorncroft 2015). Both the AMIP and historical simulations of CMIP5 show wet biases over northern Africa in spring; this bias is significantly reduced in high-resolution models. A possible reason is that the finer resolution weakens the excessive African Easterly wave activity over northern Africa and thus reduces rainfall (Martin and Thorncroft 2015). Over the East Asian monsoon region, the summer monsoon rainfall, particularly the Meiyu-Baiyu rainbelt, is underestimated in many contemporary models (Kang 2004; Huang et al. 2013). Therefore, the simulated contribution of summer rainfall to the annual total is also underestimated, resulting in relatively faster fractional accumulations of precipitation in spring and earlier onset of EAs. As shown in Yao et al. (2017), as resolution increases, intensified northerly flow over the central northern areas of China and southerly flow to the south of Japan is found both from the AMIP simulations in CMIP5 and in CAM5 with different resolutions. Those changes with resolution are related to the topography driven barotropic Rossby waves downstream of the Tibetan Plateau (Yao et al. 2017). However, how the in-

creased resolution affects the regional circulation remains inconclusive and deserves further investigation.

Although several consistent responses to resolution are identified across the three AGCMs considered, large differences still exist, especially over the Indian monsoon region. Large differences in the sensitivity to resolution over the Indian monsoon region were found between MetUM-GA3 and MRI-AGCM3, particularly in synoptic and intra-seasonal variability, such as monsoon low-pressure systems (Ogata et al. 2017). Those inconsistencies across models demonstrate the importance of improving physical parameterizations to reduce these systematic errors. This paper highlights the need for further multi-model comparisons to determine the added value of horizontal resolution in climate simulations.

**Acknowledgements:**

This work was jointly supported by the National Natural Science Foundation of China under grant Nos. 41420104006 and 41330423, Program of International S&T Cooperation under grant 2016YFE0102400, and the UK-China Research & Innovation Partnership Fund through the Met Office Climate Science for Service Partnership (CSSP) China as part of the Newton Fund. Nicholas P. Klingaman was funded by an Independent Research Fellowship from the Natural Environment Research Council (NE/L010976/1).

**References:**

Adler, R. et al. 2003: The version-2 global precipitation climatology project (GPCP) monthly precipitation analysis (1979-present). *J. Hydrometeorol.* 4, 1147-1167.

Berckmans Julie, Tim Woollings, Marie-Estelle Demory, Pier-Luigi Vlidale, and Malcolm Robserts, 2013: Atmospheric blocking in a high resolution climate model: influences of mean state, orography and eddy forcing, *Atmos. Sci. Let.* **14**: 34–40.

Chen J.H, S. J. Lin, 2012: Seasonal Predictions of Tropical Cyclones Using a 25-km-Resolution General Circulation Model, *Journal of Climate*. **26**:380-398.

Dong G., H. Zhang, A. Moise, L. Hanson, P. Liang, H. Ye, 2016: CMIP5 model-simulated onset, duration and intensity of the Asian summer monsoon in current and future climate. *Clim Dyn.*,**46:**355–382.DOI 10.1007/s00382-015-2588-z

Donlon C. J., Martin M., Stark J., Roberts-Jones J., Fiedler E., and Wimmer W. 2012. The Operational Sea Surface Temperature and Sea Ice Analysis (OSTIA) system, *Remote Sens. Environ.*, **116**, 140-158, doi:10.1016/j.rse.2010.10.017.

Endo H, Kitoh A, Ose T, Mizuta R, Kusunoki S (2012) Future changes and uncertainties in Asian precipitation simulated by multiphysics and multi-sea surface temperature ensemble experiments with high-resolution Meteorological Research Institute atmospheric general circulation models (MRI-AGCMs). J Geophys Res 117:D16118. doi:10.1029/2012JD017874

Higgins R. W., and W. Shi, 2001: Intercomparison of the principal modes of interannual and intraseasonal variability of the North American Monsoon System. *J. Climate*, **14**, 403-417.

Huang, D. Q., J. Zhu, Y.-C. Zhang, and A.-N. Huang, 2013: Uncertainties on the simulated

summer precipitation over eastern China from the CMIP5 models. J. Geophys. Res. Atmos., 118, 9035–9047

Huffman G. J., D. T. Bolvin, E. J. Nelkin, D. B. Wolff, R. F. Adler, G. Gu, Y. Hong, K. P. Bowman, and E. F. Stocker. 2007: The TRMM multisatellite precipitation analysis (TMPA): Quasi-global, multiyear, combined-sensor precipitation estimates at fine scales, *J. Hydrometeorol.*, **8(1)**: 38-55.

Hung C.W, M. Yanai, 2004: Factors contributing to the Australian summer monsoon. *Q.J.R. Meteorol. Soc.*, **130**: 739-758.

Johnson SJ et al 2016: The resolution sensitivity of the South Asian monsoon and Indo-Pacific in a global 0.35° AGCM. *Clim Dyn.*, **46(3)**: 807–831

Jolliffe, I.T., and D.B. Stephenson, 2003: Forecast Verification: A Practitioner's Guide in Atmospheric Science. Wiley, Hoboken, NJ, 240 pp.

Kang, I.-S., 2004: Current status of AGCM monsoon simulations. East Asian Monsoon, C.-P. Chang, Ed., World Scientific, 301–331.

Kitoh A, Kusunoki S. 2008: East Asian summer monsoon simulation by a 20-km mesh AGCM. *Climate Dyn.*, **31:** 389-401. doi:10.1007/s00382-007-0285-2.

Krishnamurti TN, Ramanathan Y (1982) Sensitivity of the monsoon onset to differential heating. *J Atmos Sci.* **39(6)**:1290–1306

Kusunoki Shoji, 2016: Is the global atmospheric model MRI-AGCM3.2 better than the CMIP5 atmospheric models in simulating precipitation over East Asia, *Clim Dyn*, doi: 10.1007/s00382-016-3335-9.

Li, J., R. Yu, W. Yuan, H. Chen, W. Sun, Y. Zhang. 2015: Precipitation over East Asia

simulated by NCAR CAM5 at different horizontal resolutions. *Journal of Advances in Modeling Earth Systems*, **7(2)**, 774-790. DOI 10.1002/2014MS000414

Li P., T. Zhou, X. Chen, 2017: Water vapor transport for spring persistent rains over southeastern China based on five reanalysis datasets. *Climate Dynamic*s, DOI 10.1007/s00382-017-3680-3

Liu Y. M., Chan J.C., Mao J. Y., Wu G. X., 2002: The role of Bay of Bengal convection in the onset of the 1998 South China Sea summer monsoon. *Mon Weather Rev,* **130**: 2731–2744

Mao J.Y., Wu G.X., 2007: Interannual variability in the onset of the summer monsoon over eastern Bay of Bengal. *Theor Appl Climatol.*, **89**:155–170

Martin E. R., and C. Thorncroft, 2015: Representation of African Easterly Waves in CMIP5 Models, *J. Climate*, **28**, 7702-7715.

Mizielinski, M. S., M. J. Roberts, P. L. Vidale, R. Schiemann, M.-E. Demory, J. Strachan, T. Edwards, A. Stephens, B. N. Lawrence, M. Pritchard, P. Chiu, A. Iwi, J. Churchill, C. Del Cano Novales, J. Kettleborough, W. Roseblade, P. Selwood, M. Foster, M. Glover, and A. Malcolm. 2014: High resolution global climate modelling; the UPSCALE project, a large simulation campaign. *Geosci. Model Dev*., **7:** 563-591.

Mizuta R, Yoshimura H, Murakami H, Matsueda M, Endo H, Ose T, Kamiguchi K, Hosaka M, Sugi M, Yukimoto S, Kusunoki S, Kitoh A. 2012: Climate simulations using MRI-AGCM3.2 with 20-km grid. *J Meteor Soc Japan*, **90A**: 233-258. doi:10.2151/jmsj.2012-A12

Ogata T., S. J. Jonhnson, R. Shiemann, M. Demory, R. Mizuta, K. Yoshida, O. Arakawa, 2017: The resolution sensitivity of the Asian summer monsoon and its inter-model comparison between MRI-AGCM and MetUM. *Clim Dyn*, DOI 10.1007/s00382-016-

3517-5

Raia A., I. F. A. Cavalcanti, 2008: The life cycle of the South African monsoon system. *Journal of Climate,* **21**: 6227-6246.

Rayner, N. A.; Parker, D. E.; Horton, E. B.; Folland, C. K.; Alexander, L. V.; Rowell, D. P.; Kent, E. C.; Kaplan, A., 2003: Global analyses of sea surface temperature, sea ice, and night marine air temperature since the late nineteenth century *J. Geophys. Res.* **108**: 4407 10.1029/2002JD002670

Sperber KR, Annamalai H, Kang IS, Kitoh A, Moise A, Turner A, Wang B, Zhou T, 2013: The Asian summer monsoon: an inter- comparison of CMIP5 vs. CMIP3 simulations of the late 20th century. *Clim Dyn* **41**: 2711–2744

Sperber K R, Annamalai H, 2014: The use of fractional accumulated precipitation for the evaluation of the annual cycle of monsoons. *Clim Dyn.*, **43:** 3219–3244 DOI 10.1007/s00382-014-2099-3

Sultan B., S. Janicot, 2003: The West African Monsoon Dynamics. Part II: The ‘‘Pre-onset’’ and ‘‘Onset’’ of the Summer Monsoon. *Journal of Climate,* **16:** 3407-3427.

Trenberth K, Stepaniak D, and Caron J. 2000: The global monsoon as seen through the di-vergent atmospheric circulation. *Journal of Climate*, **13(22)**: 3 969-3 993.

Wang B., H. Lin 2002: Rainy season of the Asian-Pacific summer monsoon. *J Clim*., **15**: 386–398

Wang B, Ding Q. 2008: Global monsoon: dominant mode of annual variation in the trop-ics. *Dyn Atmos Oceans,* **44**:165–183. doi:10. 1016/j.dynatmoce.2007.05.002

Wu G.X., Zhang Y.S. 1998: Tibetan Plateau forcing and the situating and timing of the

Asian monsoon onset. *Mon. Wea. Rev.*, **126**: 913–927

Wu G. X., Guan Y., Liu Y.M., Yan J.H., Mao J.Y. 2012: Air–sea interaction and formation of the Asian summer monsoon onset vortex over the Bay of Bengal. *Clim Dyn.*, **38**: 261–279.

Xu J., Chan J.C. 2001: First transition of the Asian summer monsoon in 1998 and the effect of the Tibet: tropical ocean thermal contrast. *J Meteor Soc Japan*, **79**: 241–253

Yao Junchen, Tianjun Zhou, Zhun Guo, Xiaolong Chen, Liwei Zou, Yong Sun, 2017: Improved performance of High-Resolution Atmospheric Models in simulating the East-Asian Summer Monsoon Rainbelt. *Journal of Climate*, in press.

Yu, B., and J. M. Wallace, 2000: The principal mode of interannual variability of the North American Monsoon System. *J. Climate*, **13**, 2794-2800.

Zhang L., P. Wu, T. Zhou, M. Roberts, R. Schiemann, 2016: Added value of high resolution models in simulating global precipitation characteristics. *Atmospheric Science Letters*, **17**: 646-657.

Zhao M., Isaac M. Held, Shian-Jiann Lin, and Gabriel A. Vecchi. 2009: Simulations of Global Hurricane Climatology, Interannual Variability, and Response to Global Warming Using a 50-km Resolution GCM. *J. Climate*, **22**: 6653-6678. doi: http://dx.doi.org/10.1175/2009JCLI3049.1

Zhou Tianjun, Xiaolong Chen, Bo Wu, Zhun Guo, Yong Sun, Liwei Zou, Wenmin Man, Lixia Zhang, Chao He, 2017: A Robustness Analysis of CMIP5 Models over the East Asia-Western North Pacific Domain, *Engineering*, 3(5), 773-778, https://doi.org/10.1016/J.ENG.2017.05.018

Zou, L. W., and T. J. Zhou, 2015: Asian summer monsoon onset in simulations and CMIP5 projections using four Chinese climate models. *Adv. Atmos. Sci.*, **32(6)**: 794-806.

**Figure Captions**:

**Table 1** Model descriptions including model resolution, sea surface temperature (SST) forcing, realization numbers and selected simulation years.

**Table 2.** Schematic contingency table for computing the ETS metric for model simulations of the monsoon domain (after Table 3.1 in Jolliffe and Stephenson 2003)

**Figure 1** Spatial distributions of the difference between low-resolution models and TRMM (units: mm day$^{-1}$, left column) and between high and low resolutions of the same model (units: mm day$^{-1}$, right column) in simulating annual mean precipitation. (a) MetUM-GA3 N216 minus TRMM, (b) MetUM-GA3 N512 minus MetUM-GA3 N216, (c) MRI-AGCM3-2H minus TRMM, (d) MRI-AGCM3-2S minus MRI-AGCM3-2H, (e) GFDL-HiRAM-C180 minus TRMM, (f) GFDL-HiRAM-C360 minus GFDL-HiRAM-C180. Blue lines in the left and right columns show the climatological mean precipitation from TRMM and the low-resolution models, respectively. The hatched area denotes where precipitation exceeds 7mm day$^{-1}$.

**Figure 2** As in Figure 1, but for the spatial distribution of the solstitial mode (unit: mm day$^{-1}$), defined as the difference between June-September (JJAS) and December-March (DJFM) mean precipitation. The blue and red lines indicate positive and negative values, respectively.

**Figure 3** As in Figure 1, but for the equinoctial asymmetric mode defined as the difference between April-May (AM) and October-November (ON) mean precipitation.

**Figure 4** Scatter diagrams for the fidelity of simulated precipitation and 850hPa winds of (a)-(c) annual mean, (d)-(f) solstitial mode, and (g)-(i) equinoctial asymmetric mode against TRMM and CFSR. The abscissa and ordinate are the pattern correlation coefficients (PCC) and root-mean-square-error (RMSE), respectively. The fidelity of GPCP and NCEP2 against TRMM and CFSR are also shown in dots to represent the observa-

tional uncertainty. The stars, triangles and diamonds represent the results from MetUM-GA3, MRI-AGCM3 and GFDL-HiRAM, respectively, with high-resolution models in red and low-resolution in blue.

**Figure 5** Climatological annual range of precipitation (shaded, units: mm day-1) and global monsoon domain (contours) derived from (a) TRMM, (b) GPCP, (c) MetUM-GA3 N216, (d) MetUM-GA3 N512, (e) MRI-AGCM3-2H, (f) MRI-AGCM3-2S, (g) GFDL-HiRAM-C180, (h) GFDL-HiRAM-C360. The annual range is defined as the May to September (MJJAS) minus November to March (NDJFM) mean precipitation for the Northern Hemisphere, and NDJFM minus MJJAS for the Southern Hemisphere.

**Figure 6.** The ETS score of monsoon domain simulation over (a) global (GM), (b) Indian (India), (c) Southeast Asia (SAs), (d) East Asian (EAs), (e) Australian (Aus), (f) West African (WAf), (g) South African (SAf), (h) North American (NAm) and (i) South American (SAm) monsoon. The abscissa (ordinate) is ETS scores of simulated domain derived from precipitation (U850), respectively. The fidelity of GPCP against TRMM is shown in dots. The fidelity of GPCP and NCEP2 against TRMM and CFSR are also shown in dots to represent the observational uncertainty. The star, triangle and diamond represent the results from MetUM-GA3, MRI-AGCM3 and GFDL-HiRAM, respectively, with high-resolution models in red and low-resolution in blue.

**Figure 7** Observed and simulated precipitation accumulations (unit: mm) from the first pentad to the end of year, and fractional accumulations (unit: %) around the monsoon onset pentad averaged over (a) Indian (India), (b) Southeast Asian (SAs), (c) East Asian (EAs), (d) Australian (Aus), (e) West African (WAf), (f) South African (SAf), (g) North American (NAm) and (h) South American (SAm) monsoon. Note: for Southern Hemisphere locations (Australian, South African, and South American monsoons) the pentads were reordered to July–June prior to the analysis. The black, red, blue and green

lines represent the results of TRMM, MetUM-GA3, MRI-AGCM3 and GFDL-HiRAM, respectively, with high-resolution configurations in solid lines and low-resolution configuratiosn in dashed lines.

**Figure 8** Climatological monsoon onset pentad derived from (a) TRMM, (b) GPCP, (c) MetUM-GA3 N216, (d) MetUM-GA3 N512, (e) MRI-AGCM3-2H, (f) MRI-AGCM3-2S, (g) GFDL-HiRAM-C180, (h) GFDL-HiRAM-C360. The monsoon onset pentad is defined as the pentad when fractional accumulation first becomes >=0.2 (Sperber and Annamalai 2014). Note: for Southern Hemisphere locations (Australian, South African, and South American monsoon) the pentads were reordered to July–June prior to the analysis.

**Figure 9** As in Figure 8, but for the monsoon withdrawal pentad, defined as the pentad with fractional accumulation first becomes >=0.8 (Sperber and Annamalai 2014). Note: for Southern Hemisphere locations (Australian, South African, and South American monsoon) the pentads were reordered to July–June prior to the analysis.

**Figure 10** The monsoon onset (x axis) and withdraw pentad (y axis) averaged over (a) Indian (India), (b) Southeast Asian (SAs), (c) East Asian (EAs), (d) Australian (Aus), (e) West African (WAf), (f) South African (SAf), (g) North American (NAm) and (h) South American (SAm) monsoon. Note: for Southern Hemisphere locations (Australian, South African, and South American monsoon) the pentads were reordered to July–June prior to the analysis. The dots, stars, triangles and diamonds represent the results from the observations, MetUM-GA3, MRI-AGCM3 and GFDL-HiRAM, respectively, with high-resolution configurations in red and low-resolution configurations in blue.

**Figure 11** Improvement of the simulation on the annual cycle of global monsoon precipitation with horizontal resolution. Red boxes indicate high-resolution consistently improves performance across all three AGCMs; blue boxes indicate improvements with

resolution are inconsistent; orange boxes indicate a better simulation is shown in all three high-resolution AGCMs but the responses to resolution are inconsistent across models. The values from left to right in each box are the difference between high- and low-resolution configurations of MetUM-GA3, MRI-AGCM3 and GFDL-HiRAM, respectively. The metric for the annual modes, including annual mean (ANN), solstitial mode (AC1), the equinoctial asymmetric mode (AC2), is the pattern correlation coefficient with TRMM. The metrics for the monsoon domain and monsoon onset/withdrawal are ETS and the onset/withdrawal pentad, respectively.

**Table 1. Model information description including model resolution, sea surface temperature (SST) forcing, realization numbers and selected simulation years.**

| Model | Resolution | SST | Realizations | Selected Years |
|---|---|---|---|---|
| MetUM-GA3 | N216 (0.83°x0.55°) | OSTIA | 3 | 1998-2008 |
| | N512 (0.35°x0.23°) | OSTIA | 5 | 1998-2008 |
| GFDL-HiRAM | C180(0.625°x0.5°) | HadISST1 | 3 | 1998-2008 |
| | C360(0.31°x0.25°) | HadISST1 | 2 | 1998-2008 |
| MRI-AGCM3 | 2H(0.56°x0.56°) | HadISST1 | 2 | 1998-2008 |
| | 2S(0.18°x0.18°) | HadISST1 | 1 | 1998-2008 |

699 **Table 2. Schematic contingency table for computing the ETS metric for model**
700 **simulations of the monsoon domain (after Table 3.1 in Jolliffe and Stephenson 2003)**

| | **Event Observed** | | |
|---|---|---|---|
| **Event Simulated** | **Monsoon domain** | **Non-monsoon domain** | **Total** |
| **Monsoon domain** | a (Hits) | b (False alarms) | a+b |
| **Non-monsoon domain** | c (Misses) | d (Correct rejections) | c+d |
| **Total** | a+c | b+d | a+b+c+d=n |

701
702
703
704

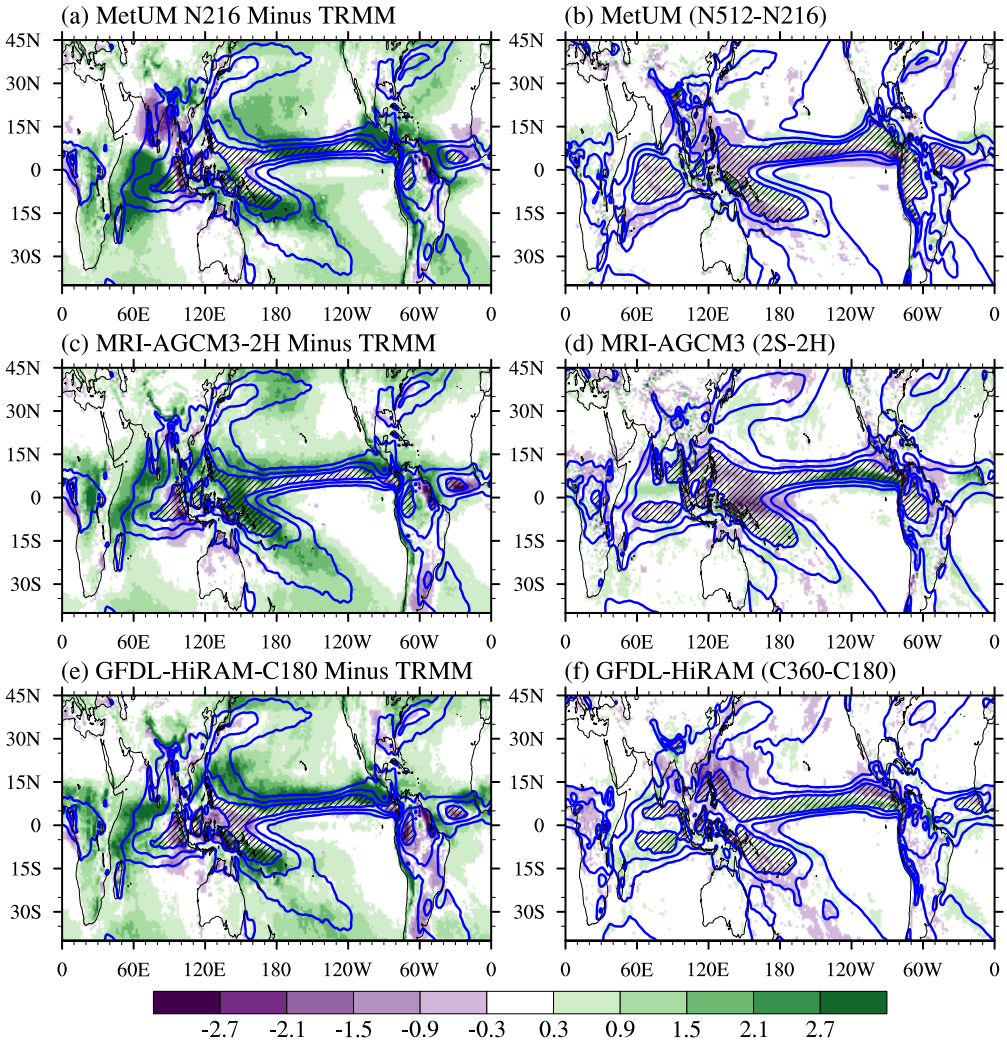


**Figure 1** Spatial distributions of the difference between low-resolution models and TRMM (units: mm day$^{-1}$, left column) and between high and low resolutions of the same model (units: mm day$^{-1}$, right column) in simulating annual mean precipitation. (a) MetUM-GA3 N216 minus TRMM, (b) MetUM-GA3 N512 minus MetUM-GA3 N216, (c) MRI-AGCM3-2H minus TRMM, (d) MRI-AGCM3-2S minus MRI-AGCM3-2H, (e) GFDL-HiRAM-C180 minus TRMM, (f) GFDL-HiRAM-C360 minus GFDL-HiRAM-C180. Blue lines in the left and right columns show the climatological mean precipitation from TRMM and the low-resolution models, respectively. The hatched area denotes where precipitation exceeds 7mm day$^{-1}$.

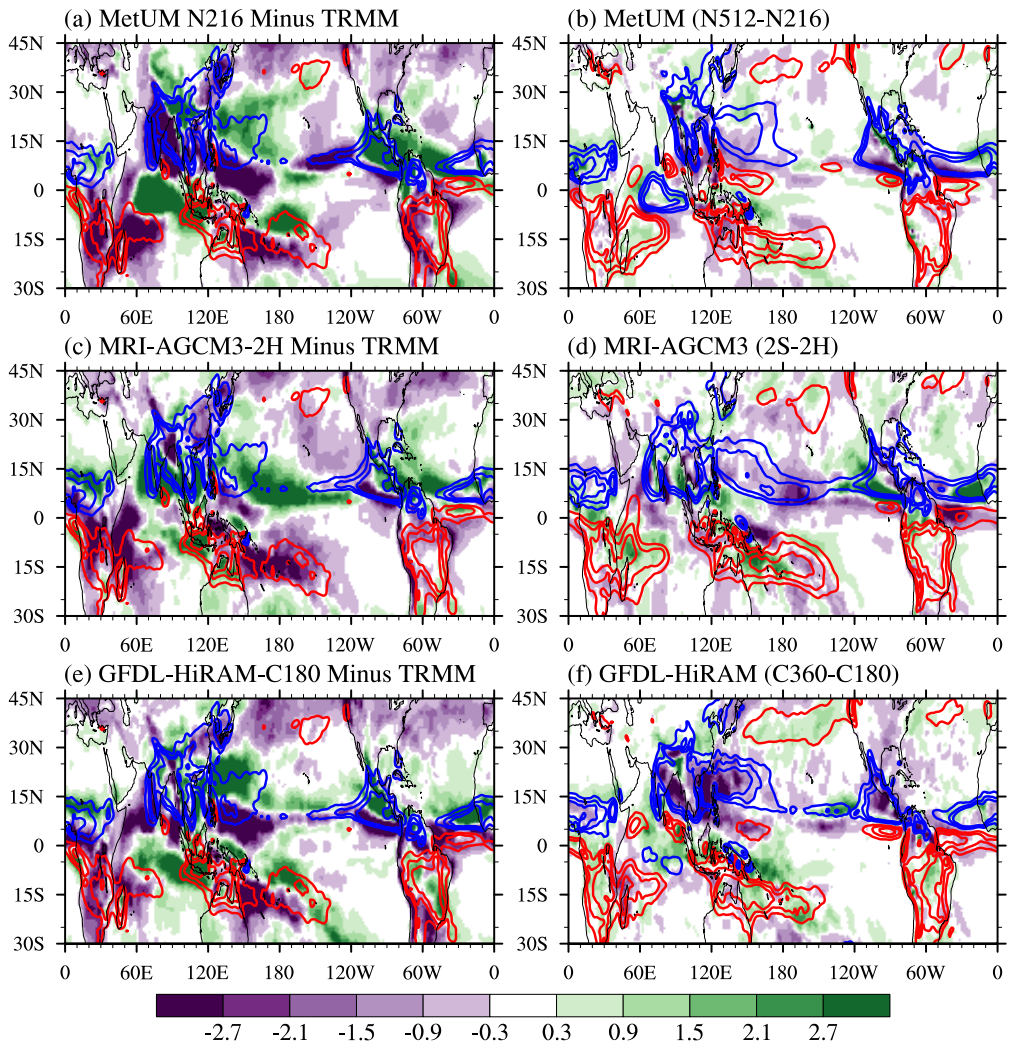


716

717 **Figure 2** As in Figure 1, but for the spatial distribution of the solstitial mode (unit: mm

718 day$^{-1}$), defined as the difference between June-September (JJAS) and December-March

719 (DJFM) mean precipitation. The blue and red lines indicate positive and negative values,

720 respectively.

721

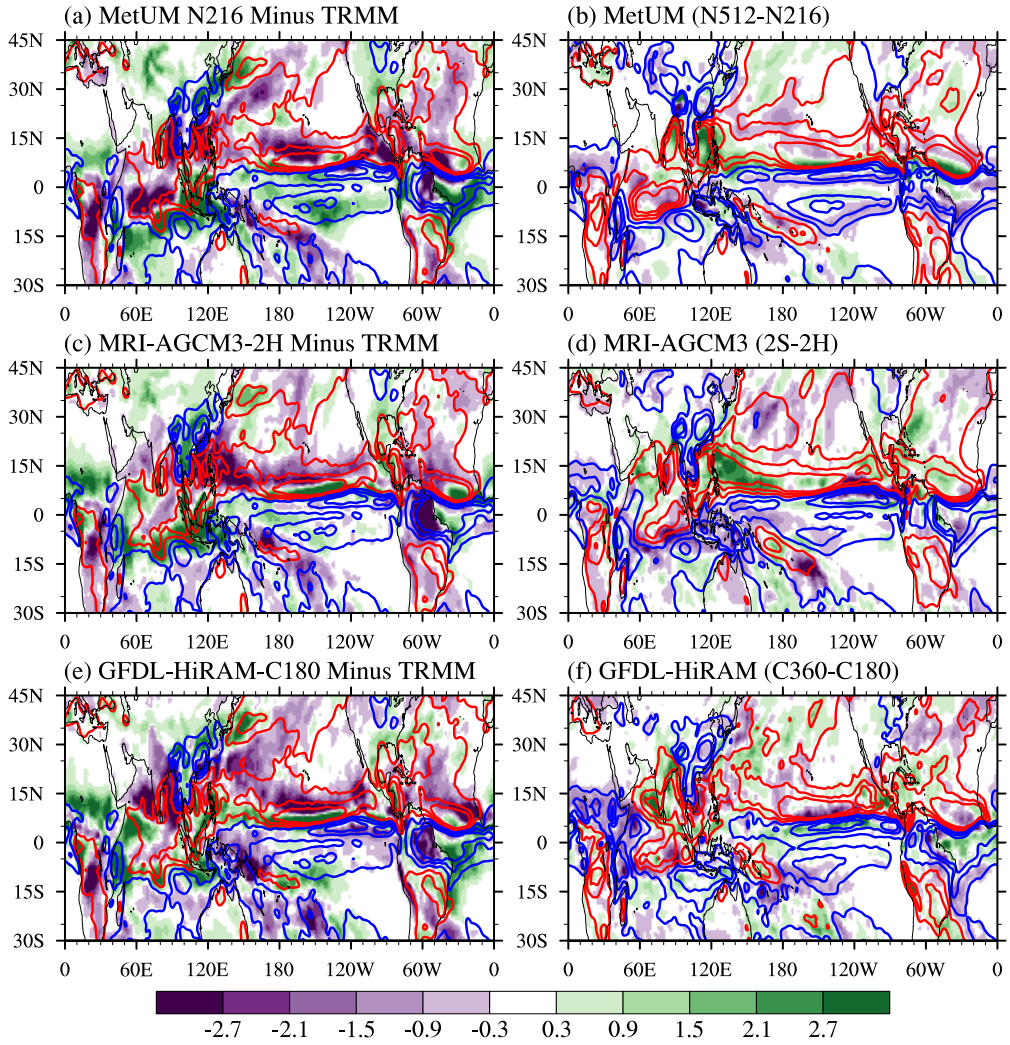


**Figure 3.** As in Figure 1, but for the equinoctial asymmetric mode defined as the difference between April-May (AM) and October-November (ON) mean precipitation.

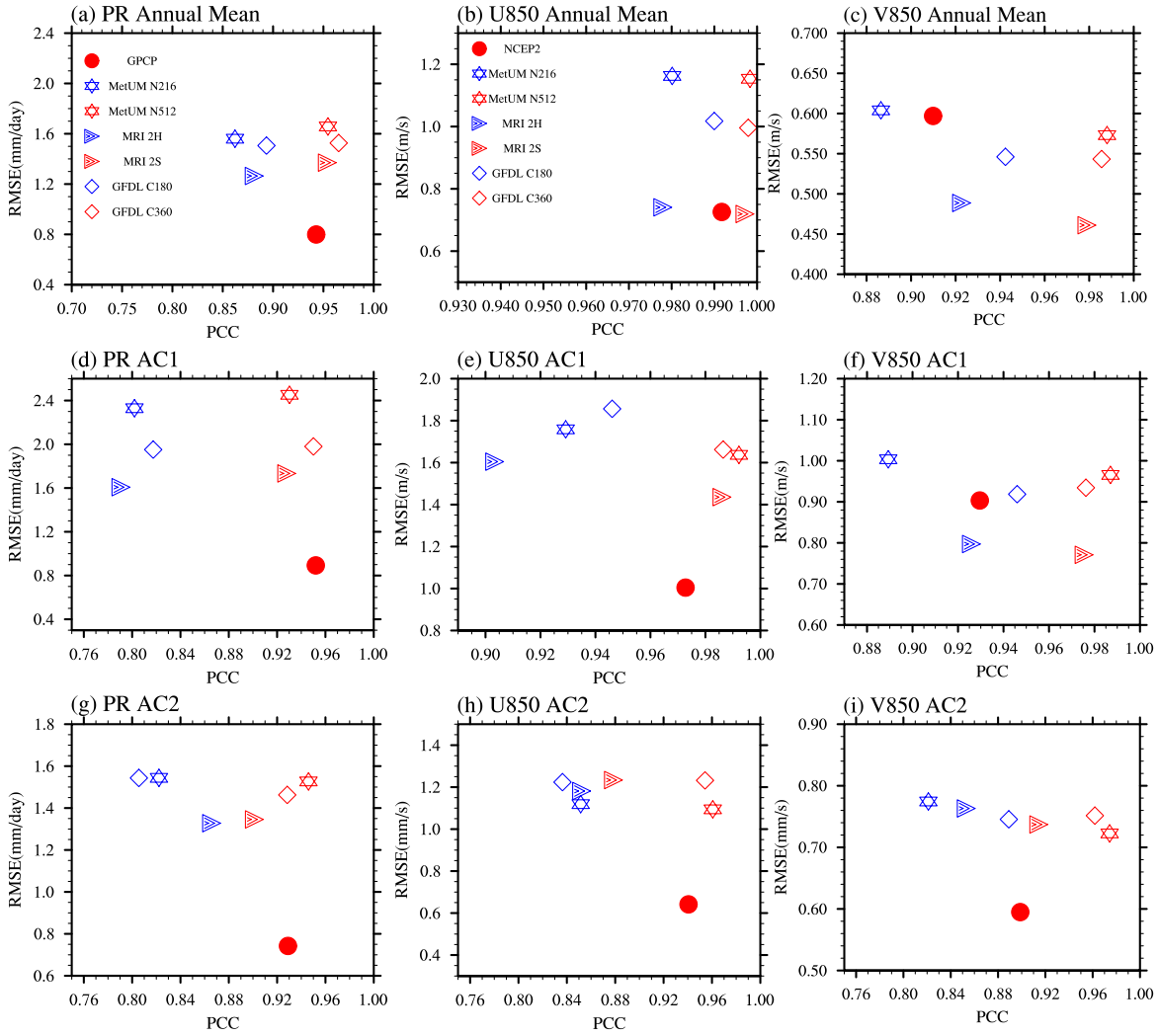


**Figure 4** Scatter diagrams for the fidelity of simulated precipitation and 850hPa winds of (a)-(c) annual mean, (d)-(f) solstitial mode, and (g)-(i) equinoctial asymmetric mode against TRMM and CFSR. The abscissa and ordinate are the pattern correlation coefficients (PCC) and root-mean-square-error (RMSE), respectively. The fidelity of GPCP and NCEP2 against TRMM and CFSR are also shown in dots to represent the observational uncertainty. The stars, triangles and diamonds represent the results from MetUM-GA3, MRI-AGCM3 and GFDL-HiRAM, respectively, with high-resolution configurations in red and low-resolution configurations in blue.

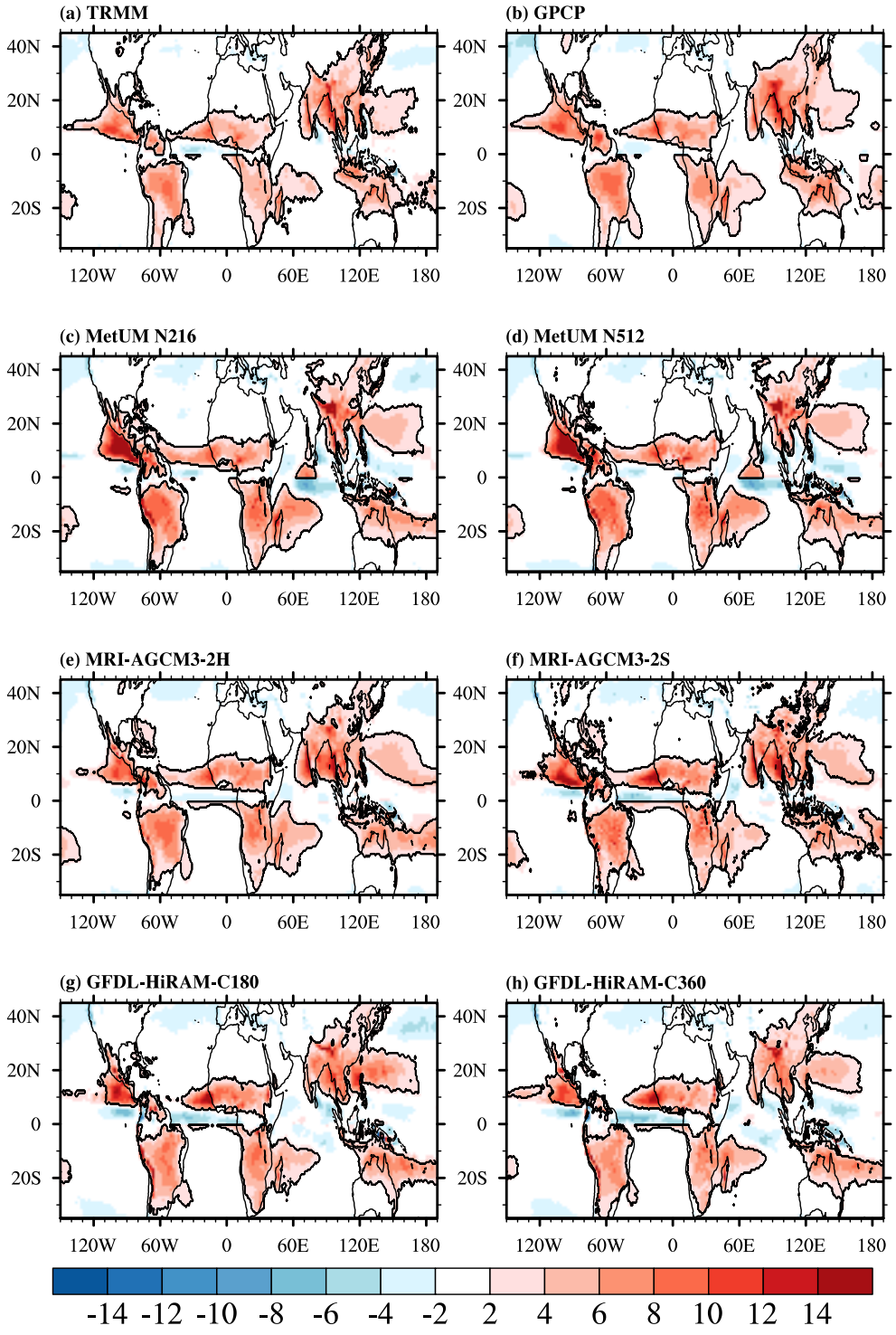


**Figure 5** Climatological annual range of precipitation (shaded, units: mm day-1) and global monsoon domain (contours) derived from (a) TRMM, (b) GPCP, (c) MetUM-GA3 N216, (d) MetUM-GA3 N512, (e) MRI-AGCM3-2H, (f) MRI-AGCM3-2S, (g) GFDL-HiRAM-C180, (h) GFDL-HiRAM-C360. The annual range is defined as the May to September (MJJAS) minus November to March (NDJFM) mean precipitation for the Northern Hemisphere, and NDJFM minus MJJAS for the Southern Hemisphere.

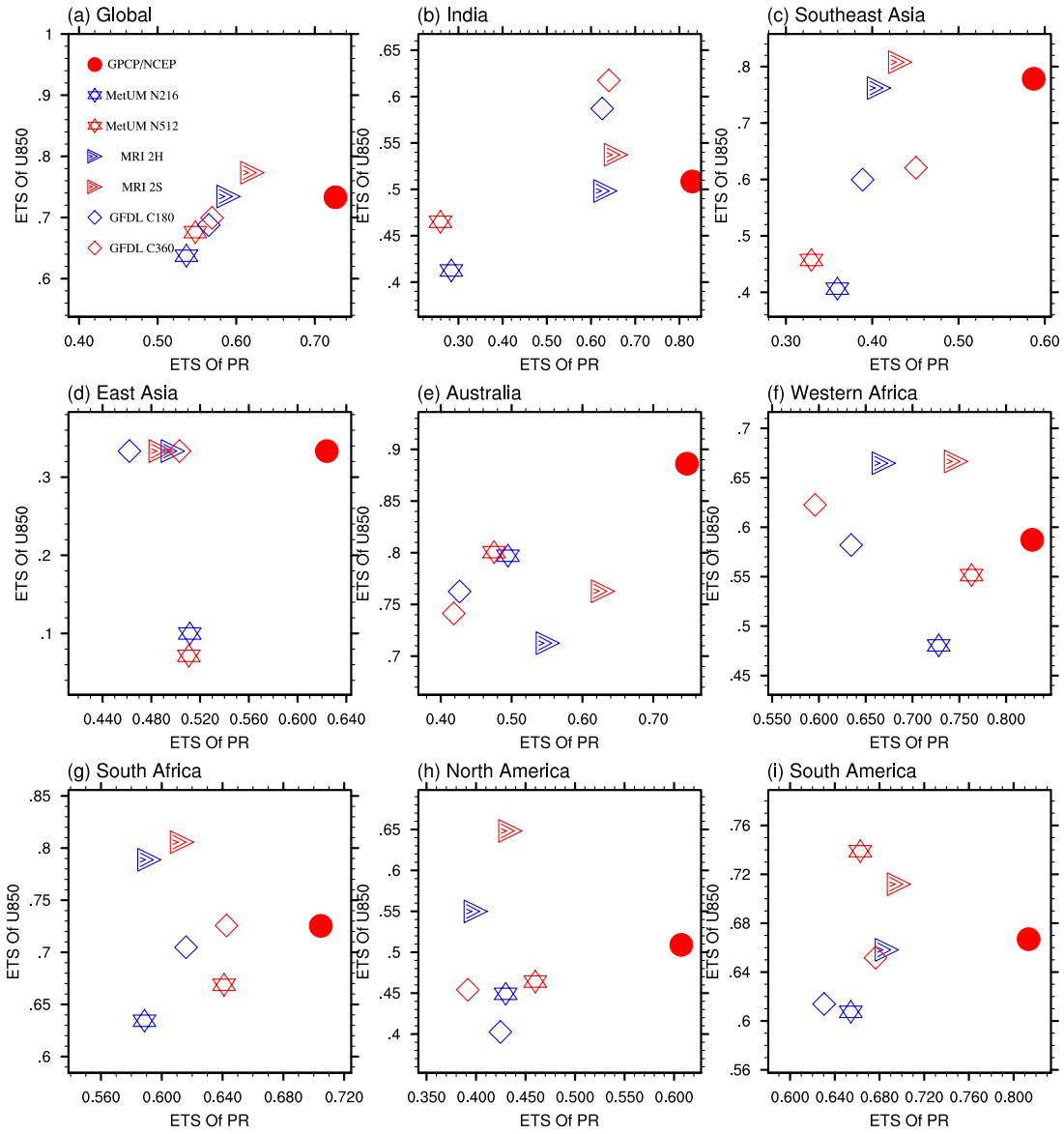


**Figure 6.** The ETS score of monsoon domain simulation over (a) global (GM), (b) Indian (India), (c) Southeast Asian (SAs), (d) East Asian (EAs), (e) Australian (Aus), (f) West African (WAf), (g) South African (SAf), (h) North American (NAm) and (i) South American (SAm) monsoon. The abscissa (ordinate) is ETS scores of simulated domain derived from precipitation (U850). The fidelity of GPCP against TRMM is shown in dots. The fidelity of GPCP and NCEP2 against TRMM and CFSR are also shown in dots to represent the observational uncertainty. The star, triangle and diamond represent the results from MetUM-GA3, MRI-AGCM3 and GFDL-HiRAM, respectively, with high-resolution configurations in red and low-resolution configurations in blue.

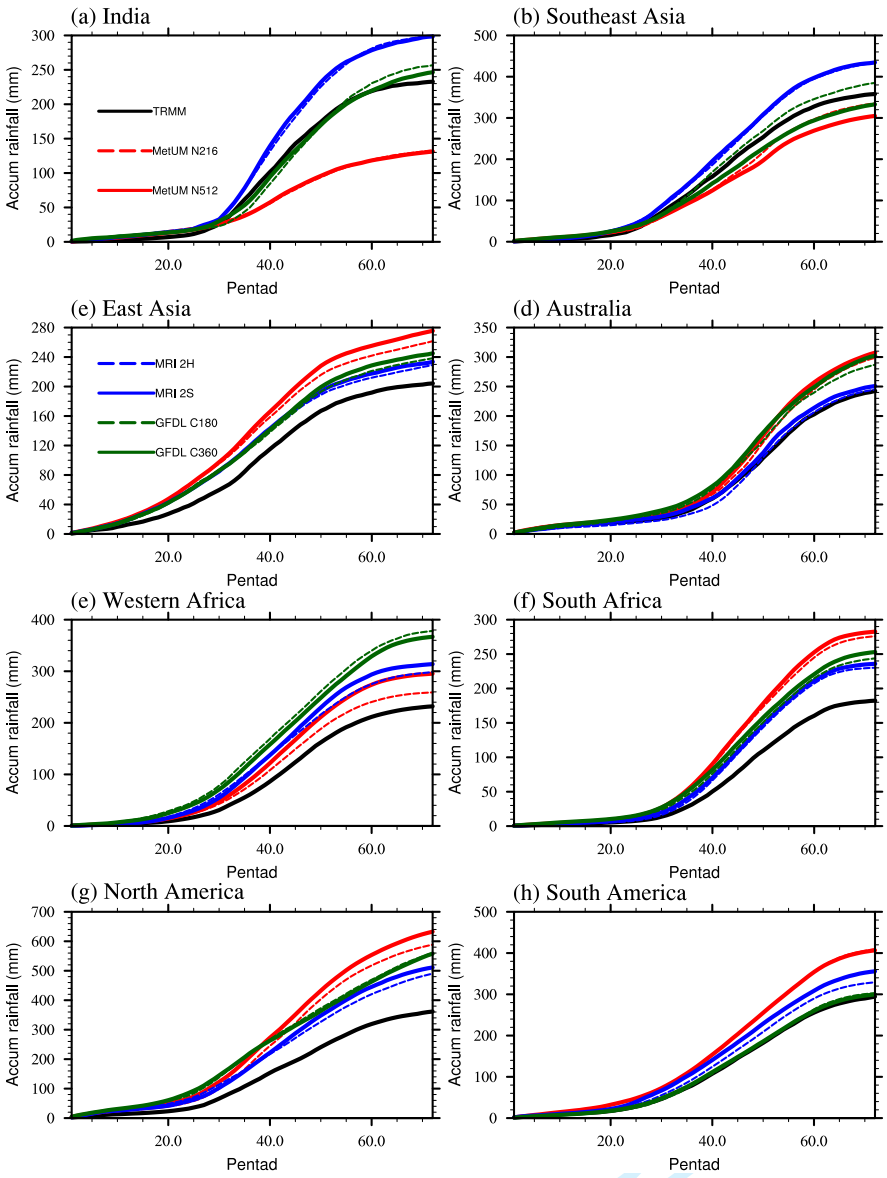


**Figure 7** Observed and simulated precipitation accumulations (unit: mm) from the first pentad to the end of year, and fractional accumulations (unit: %) around the monsoon onset pentad averaged over (a) Indian (India), (b) Southeast Asian (SAs), (c) East Asian (EAs), (d) Australian (Aus), (e) West African (WAf), (f) South African (SAf), (g) North American (NAm) and (h) South American (SAm) monsoon. Note: for Southern Hemisphere locations (Australian, South African, and South American monsoons) the pentads were reordered to July–June prior to the analysis. The black, red, blue and green lines represent the results of TRMM, MetUM-GA3, MRI-AGCM3 and GFDL-HiRAM, respectively, with high-resolution configurations in solid lines and low-resolution configuratiosn in dashed lines.

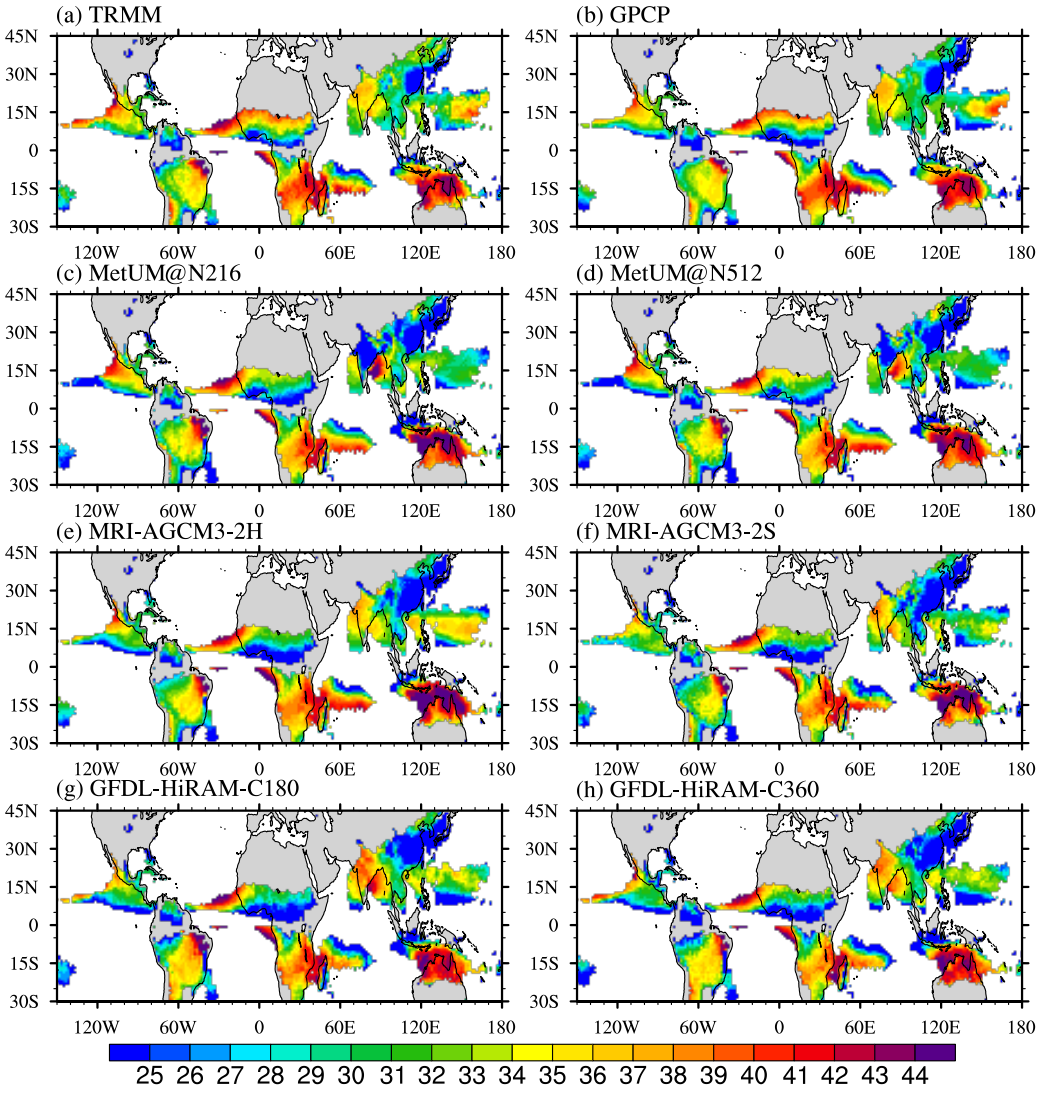


**Figure 8** Climatological monsoon onset pentad derived from (a) TRMM, (b) GPCP, (c) MetUM-GA3 N216, (d) MetUM-GA3 N512, (e) MRI-AGCM3-2H, (f) MRI-AGCM3-2S, (g) GFDL-HiRAM-C180, (h) GFDL-HiRAM-C360. The monsoon onset pentad is defined as the pentad when fractional accumulation first becomes >=0.2 (Sperber and Annamalai 2014). Note: for Southern Hemisphere locations (Australian, South African, and South American monsoon) the pentads were reordered to July–June prior to the analysis.

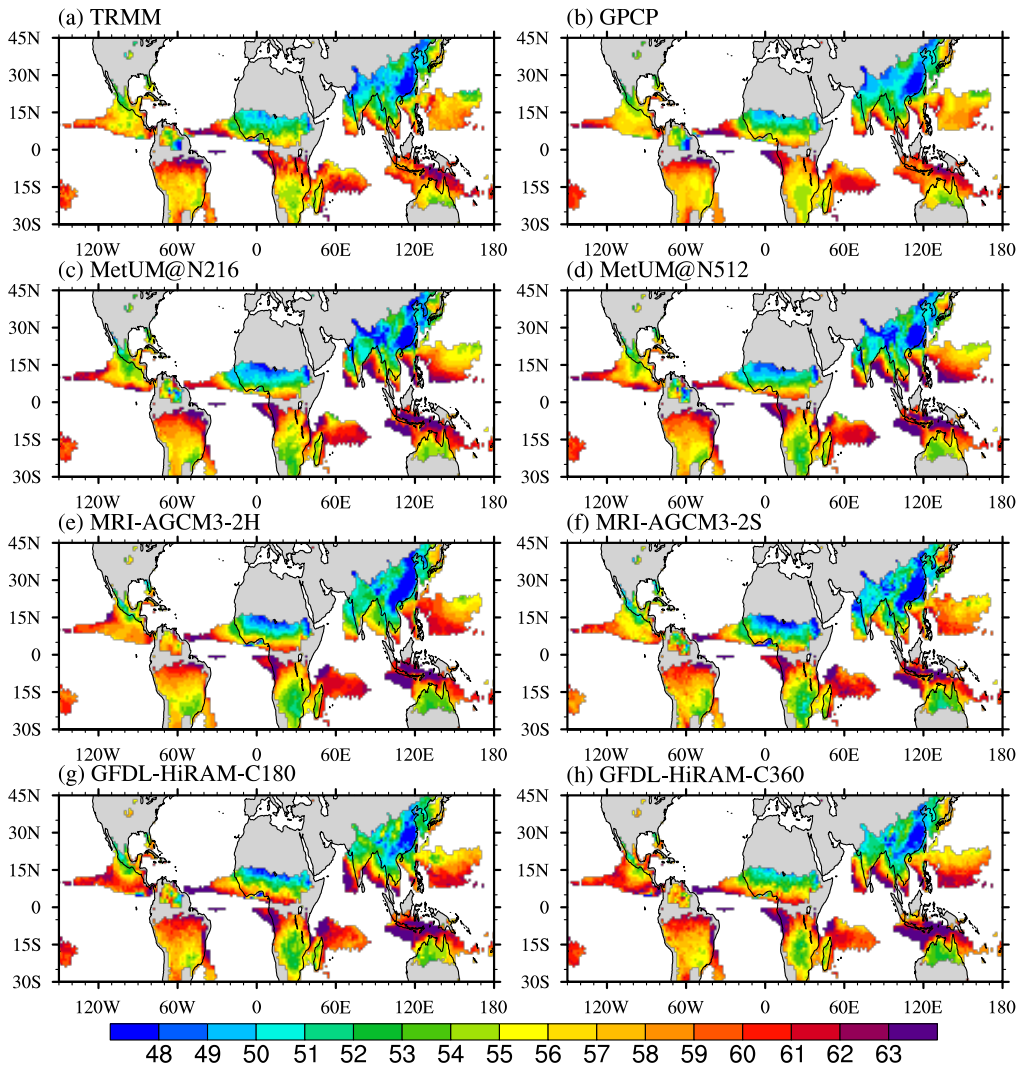


**Figure 9** As in Figure 8, but for the monsoon withdrawal pentad, defined as the pentad with fractional accumulation first becomes >=0.8 (Sperber and Annamalai 2014). Note: for Southern Hemisphere locations (Australian, South African, and South American monsoon) the pentads were reordered to July–June prior to the analysis.

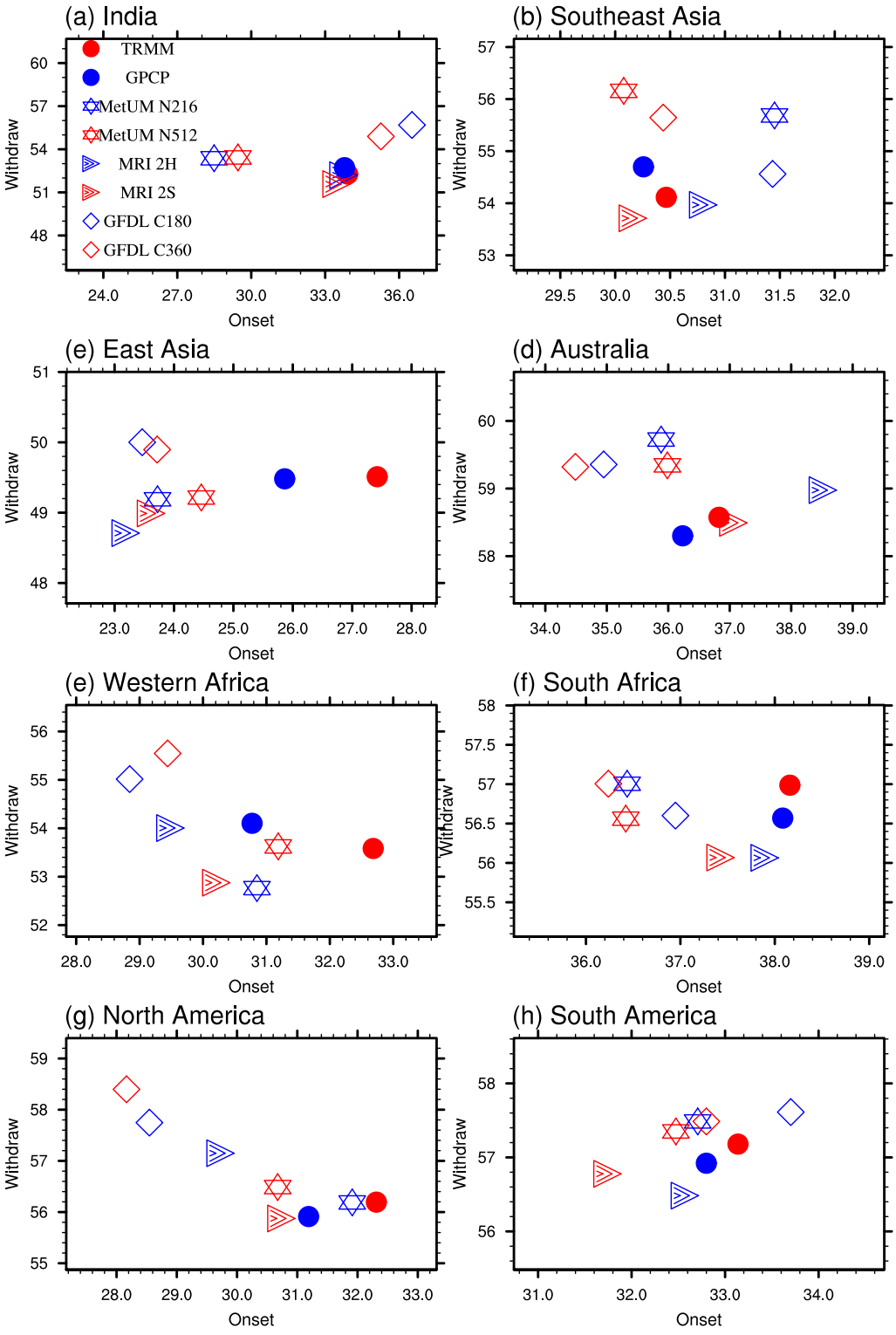


**Figure 10.** The monsoon onset (x axis) and withdraw pentad (y axis) averaged over (a) Indian (India), (b) Southeast Asian (SAs), (c) East Asian (EAs), (d) Australian (Aus), (e) West African (WAf), (f) South African (SAf), (g) North American (NAm) and (h) South American (SAm) monsoon. Note: for Southern Hemisphere locations (Australian, South

African, and South American monsoon) the pentads were reordered to July–June prior to the analysis. The dots, stars, triangles and diamonds represent the results from the observations, MetUM-GA3, MRI-AGCM3 and GFDL-HiRAM, respectively, with high-resolution configurations in red and low-resolution configurations in blue.

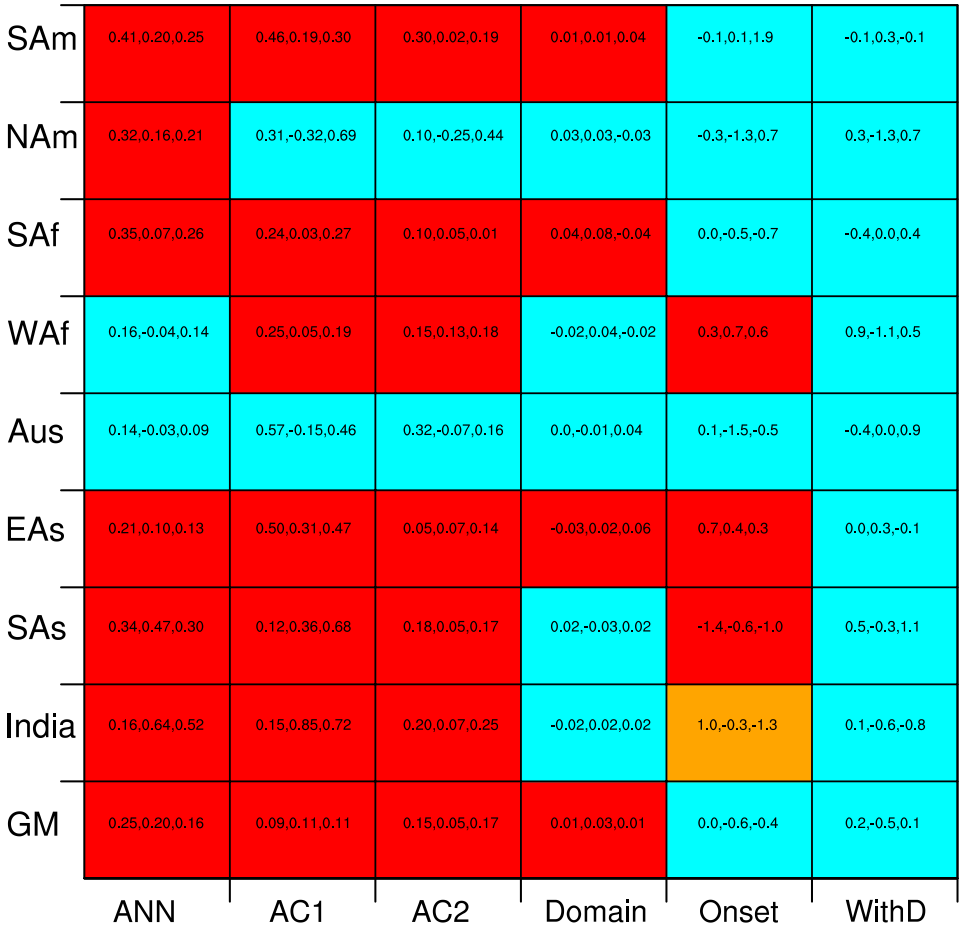


**Figure 11** Improvement of the simulation on the annual cycle of global monsoon precipitation with horizontal resolution. Red boxes indicate high-resolution consistently improves performance across all three AGCMs; blue boxes indicate improvements with resolution are inconsistent; orange boxes indicate a better simulation is shown in all three high-resolution AGCMs but the responses to resolution are inconsistent across models. The values from left to right in each box are the difference between high- and low-resolution configurations of MetUM-GA3, MRI-AGCM3 and GFDL-HiRAM, respectively. The metric for the annual modes, including annual mean (ANN), solstitial mode (AC1), the equinoctial asymmetric mode (AC2), is the pattern correlation coefficient with TRMM. The metrics for the monsoon domain and monsoon onset/withdrawal are ETS and the onset/withdrawal pentad, respectively.